

Temperature Controlled Fabrication of TiO₂ Nanotube-Based Arrays Electrode and Its Application for Photoelectrocatalytic Degradation of RhB

J Wu^{1,2}, K Zhu², Y. F. Guo¹, H Xu^{1,*}, W Yan¹

¹ Department of Environmental Science and Engineering, Xi'an Jiaotong University, Xi'an 710049, China

² Xi'an XD Switchgear Electric Co., Ltd., Xi'an 710049, China

*E-mail: xuhao@xjtu.edu.cn

Received: 5 October 2019 / Accepted: 16 November 2019 / Published: 31 December 2019

TiO₂ nanotube arrays electrodes at different temperature were successfully synthesized via anodization method. The as-prepared samples were characterized by FE-SEM, XRD, I-V curve, I-t curve, EIS and Mott-Shottky measurement. The FE-SEM and XRD results showed that temperature could affect the surface morphology, nanotube length and crystal structure of the electrodes. The photoelectrochemical measurements revealed that the photocurrent, flat band potential (V_{fb}), donor concentration (N_D) and the width of the space charge layer (W_{sc}) varied with the temperature. Rhodamine B (RhB) degradation experiment was conducted to investigate the photoelectrocatalytic activity of the electrodes. It was found that the electrode fabricated at 30°C exerted the best catalytic activity and a strong reusability. The enhanced catalytic activity could be attributed to its fast charge transport and increased electrons-holes separation efficiency. Moreover, the main reactive species and degradation mechanism during the photoelectrocatalytic degradation process were also studied. It was observed that holes (h^+), $\cdot OH$ and $\cdot O_2^-$ benefited RhB degradation. Finally, a possible RhB degradation mechanism during the photoelectrodegradation was proposed. The results provided a specific RhB degradation pathway for photoelectrodegradation. These findings gave us a great insight to understand the property and photoelectrocatalytic process on TiO₂ nanotube arrays.

Keywords: TiO₂ nanotube arrays, Temperature, Photoelectrocatalytic, RhB degradation mechanism

1. INTRODUCTION

Highly ordered TiO₂ nanotube arrays electrode was regarded as the most potential photocatalyst for its excellent charge transport performance, photostability and large surface area[1-4]. The particular nanotube structure provides a pathway for charge transfer and accelerates the separation of electrons-holes pairs[5, 6]. These advantages make the TiO₂ nanotube arrays be widely used in water splitting[7-

9], dye-sensitized cells[10-12], sensors[13-16] and pollutant degradation[17-20]. According to the literature, the surface properties and the charge transfer are the important factors for the catalytic reaction[21-23]. Many factors (i.e. potential, time, electrolyte composition) that affect the TiO₂ nanotube arrays during the preparation process were extensively studied[24-27]. Some architecture parameters such as wall thickness, pore diameter, roughness and nanotube length were also investigated to enhance the catalytic activity[28-30]. However, seldom research was carried out to discuss the effect of temperature on the fabrication and performance of TiO₂ nanotube arrays. Intensive study in terms of the specific photoelectrocatalytic process was further acquired.

During the past years, degradation of dyes in wastewater have attracted much attention because of its strong toxicity, poor biodegradation and high field. Rhodamine B (RhB) is a representative cationic dye and has been widely used as a colorant in textile industry. Photocatalysis technology was proved to be a more favorable approach than others due to its low cost, environmental friendliness and high efficiency[31-33]. The photoelectrocatalysis technology based on photocatalysis gains extensive attention because the applied bias can improve the separation efficiency of electrons-holes pairs. Many efforts have been devoted to understanding the photocatalytic degradation of dyes[34]. However, the specific photoelectrodegradation mechanism still requires further improvement of the photoelectrocatalytic performance.

In this work, TiO₂ nanotube arrays electrodes at different temperature were prepared via oxidation approach. Then the photoelectrochemical measurements including I-V curve, I-t curve, electrochemical impedance spectroscopy (EIS) and Mott-Shottky were carried out to investigate the photoelectrocatalytic process. Moreover, the main reactive species and specific degradation mechanism during the RhB photoelectrodegradation were also studied. It is expected that these findings can provide a great insight to research the photoelectrocatalytic degradation process.

2. EXPERIMENTAL DETAILS

2.1. Temperature controlled preparation of TiO₂ nanotube arrays

The Ti foils (20 mm×40 mm size, 0.5 mm thickness, 99.6% purity, BaoTi Co.Ltd, China) were ultrasonically cleaned in isopropanol, ethanol and deionized water in turn for 30 min, and then dried in an oven at 40°C. Anodization experiments were performed on a two-electrode configuration with titanium sheet as the counter electrode at different temperature (30°C/40°C/50°C/60°C). The temperature was controlled by a thermostatic waterbath, as shown in Fig. 1. The samples obtained at different temperature were marked as T-30°C, T-40°C, T-50°C and T-60°C, respectively. Anodization was carried out in the electrolyte containing 97 vol% EG and 3 vol% deionized water with 0.3 wt% NH₄F. The applied voltage was kept at 50 V with magnetic agitation. After anodization, the as-synthesized samples were rinsed with deionized water and then subjected to ultrasonication to remove the sediment. Finally, the as-prepared amorphous TiO₂ nanotube arrays samples were annealed at 500°C in air for 2 h to induce crystallization (the heating and cooling rate were both 1°C/min).

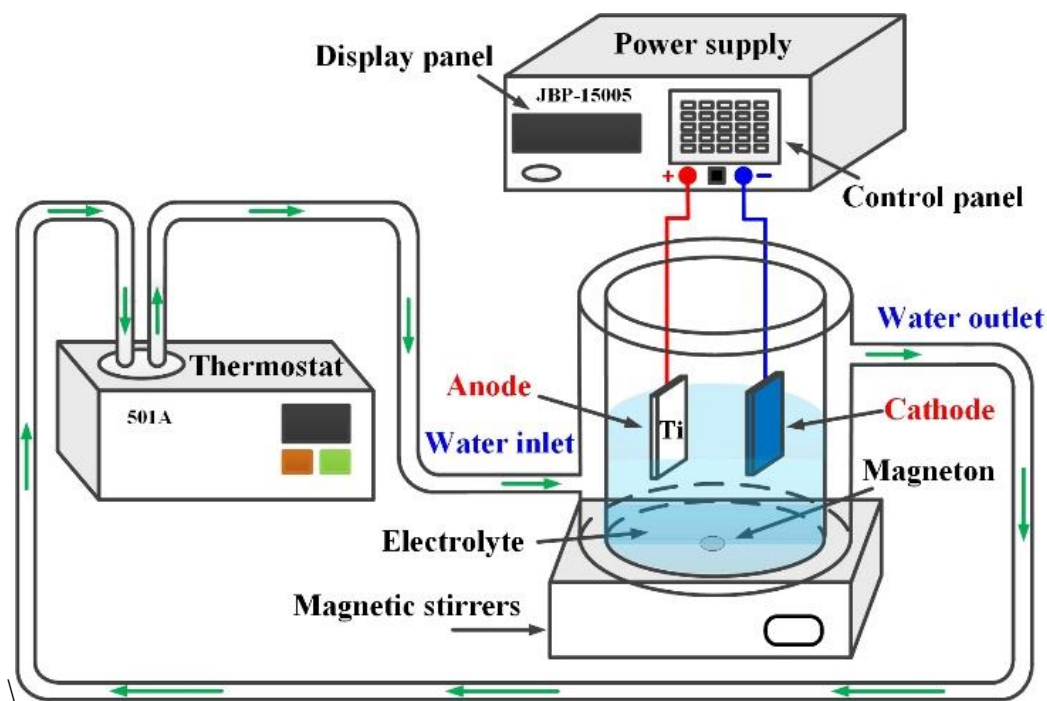


Figure 1. Illustration of temperature controlled electrochemical cell in which the Ti foils are anodized

2.2 Characterization

The surface morphology and cross-section structure of the as-synthesized samples was characterized by a field-emission scanning electron microscopy (FE-SEM, JEOL, JSM-6700F). X-ray diffraction (XRD) was performed on an X'pert PRO MRD diffractometer with a scanning angle (2θ) range of 10-80°.

The photoelectrochemical performance was examined by electrochemical workstation (CHI 660D, Chenhua, Shanghai) in a three-electrode system with TiO₂ nanotube arrays as the working electrode, Pt sheet as the counter electrode, and Ag/AgCl as the reference electrode. The photocurrent-time properties were obtained in the photoelectrochemical cell (PEC) with a 375 nm LED as simulated excitation light source. The photocurrent-voltage characteristic (I-V) were carried out in 0.1 M Na₂SO₄ aqueous solutions between -0.5 V and 1.0 V. Electrochemical impedance spectroscopy (EIS) measurements were carried out to understand the charge transport properties of the electrodes. The frequency range employed was from 100 kHz to 0.1 Hz and the amplitude of sinusoidal wave was 10 mV. The Mott-Schottky measurements were performed at single frequency of 3 Hz with 10 mV amplitude, under various applied potentials.

2.3 Photoelectrocatalytic degradation experiment

The degradation process was carried out in the PEC with RhB (10 ppm) and Na₂SO₄ (0.1 M) as the supporting electrolytes. The mixture solutions were magnetically stirred for 30 min in dark to attain adsorption-desorption equilibrium between the RhB and photocatalyst before illumination. Then the

photoelectrocatalytic activity of the as-prepared samples were evaluated for RhB degradation. During this process, the applied bias was kept at 0.5 V. Moreover, the solutions were illuminated with a 375 nm LED monochromatic source placed outside the PEC. At given interval times, 10 mL solutions were sampled from the PEC. The RhB removal efficiency was determined by UV-Vis spectrophotometer (UV2600, LongNiKe Co., Ltd., China) and its maximum absorption peaks were at 554 nm. Solid phase micro-extraction-gas chromatography-mass spectrometry (SPME-GC-MS) technique was employed to analyze the intermediates in the photoelectrocatalytic degradation process. The samples that were absorbed on the SPME syringe were automatically injected into a TRACE GC Ultra (Thermo/Finnigan, Milan, Italy) gas chromatograph and a TraceISQ (Thermo/Finnigan, Milan, Italy) mass spectrometric detector. The injection port was set in splitless mode and kept at 260°C. The oven temperature was maintained at 60°C for 3 min and then ramped to 280°C at 10°C/min. The flow was set in continuous flow mode with the carrier gas (He, 99.999%) rate of 1 mL/min. The ion source temperature and interface temperature were maintained at 230°C and 280°C, respectively.

3. RESULTS AND DISCUSSION

3.1. The morphology and structure of the electrodes

The influence of temperature on surface morphology and cross-sectional structure of the electrodes were investigated by FE-SEM. As shown in Fig. 2, the surface morphology and the nanotube length of the electrode varied with the temperature. The nanotube lengths of the electrodes at different temperature were 8.66 μm (T-30°C), 11.73 μm (T-40°C), 14.05 μm (T-50°C), and 10.58 μm (T-60°C), respectively. The growth of the nanotube is dependent on the field-assisted oxidation, field-assisted migration, field-assisted dissolution and chemical dissolution [35]. The increase of the solution temperature from 30°C to 50°C accelerates the apparent reaction rate, increasing the length of the nanotube. When the temperature increases from 50°C to 60°C, the nanotube length decreased because the rate of oxide growth at Ti/TiO₂ interface was less than the rate of oxide dissolution at the pore-bottom/electrolyte interface. A smooth surface of highly ordered TiO₂ nanotube arrays electrode was obtained when the temperature was 30°C (Fig. 2b). A few nanowires appeared as the temperature increased to 40°C and the tubular structure still orderly arranged (Fig. 2d). When the temperature further raised, the surface was gradually covered by nanowires (Fig. 2f and Fig. 2h) and the nanowires/nanotube composite arrays structure was eventually formed.

The formation of nanowires that were vertically split off from the nanotubes can be explained by the bamboo-splitting model [36]. At a high potential, the hydrogen ions generated on the surface of nanotubes by electrolysis were driven to the cathode by the electric field, leading to the generation of an interface tension stress of nanotubes in the electrolyte. Chemical dissolution of nanotubes may favorably occur along with the stress, thenceforth forming the nanowires. It was found that nanotube length increased with the temperature until 50°C and then decreased, which can be attributed to the relationship between electrochemical etch rate and chemical dissolution rate.

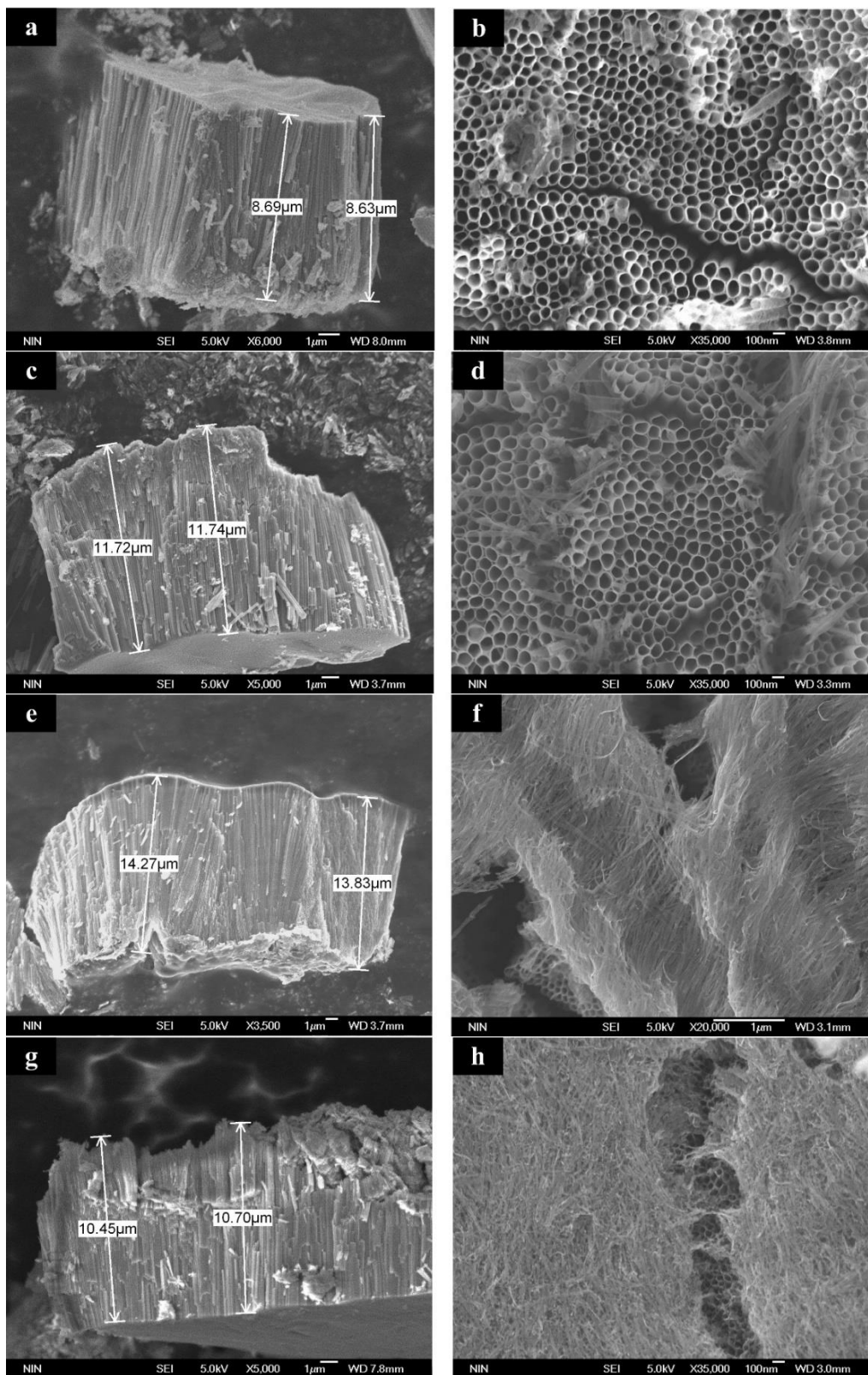


Figure 2. FE-SEM (a) the cross-sectional view and (b) top view of T-30°C; (c) the cross-sectional view and (d) top view of T-40°C; (e) the cross-sectional view and (f) top view of T-50°C; (g) the cross-sectional view and (h) top view of T-60°C

The nanotube length increased when electrochemical etch rate was higher than chemical dissolution rate ($T=30^{\circ}\text{C}/40^{\circ}\text{C}/50^{\circ}\text{C}$). On the contrary, the nanotube length decreased ($T=60^{\circ}\text{C}$).

Fig. 3 shows XRD patterns of the as-prepared samples. It was observed that temperature may affect the final crystal phase. T- 30°C , T- 40°C and T- 50°C samples exhibited the representative diffraction peaks of anatase TiO_2 . However, the main crystal face changed with the temperature. T- 30°C and T- 40°C displayed the main crystal plane of (101). As the temperature increased to 50°C , the intensity of (004) plane gradually equaled to the (101) plane. The main crystal face of T- 50°C was (004) and (101) plane. It should be noted that T- 60°C showed the diffraction peaks of rutile and anatase. As was known to all, the rutile TiO_2 was more stable than anatase TiO_2 . It could be reasonably speculated that higher temperature in the preparation process may be favorable for the formation of rutile TiO_2 in the subsequent anneal process. From Fig. 3 we also found the peaks corresponding to Ti substrate. The appearance of Ti diffraction peaks was caused by the weak binding force between the substrate and TiO_2 nanotube arrays. Some TiO_2 nanotube arrays were removed during the ultrasonication removal of surface sediments process [37]. Inversely, a strong binding force existed for the T- 30°C , T- 40°C and T- 50°C electrodes. Thus, no Ti diffraction peaks appeared for these electrodes. According to Debye-Scherrer equation, the average grain size of T- 30°C , T- 40°C , T- 50°C , and T- 60°C was 15.4 nm, 16.7 nm, 14.2 nm and 13.9 nm, respectively. This implied that the grain size first increased and then decreased with the temperature. We inferred that the generation of nanowires may minish the grain size.

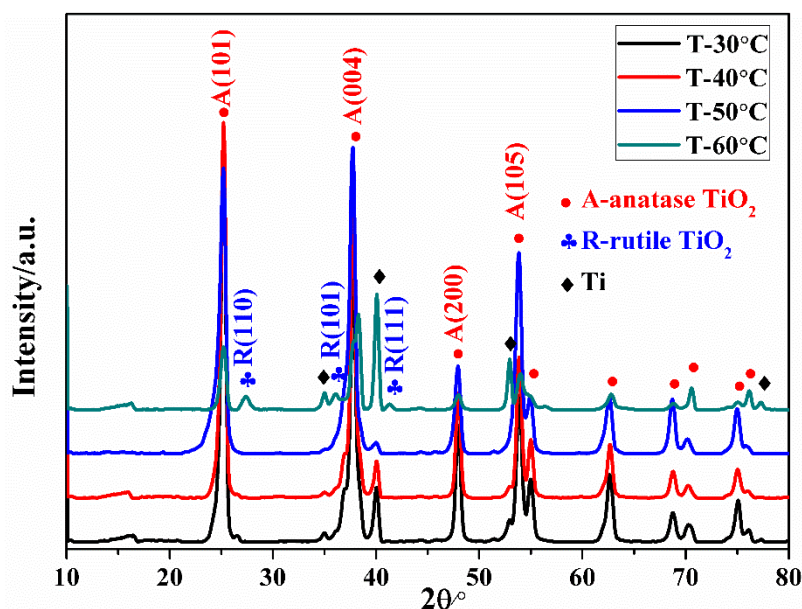


Figure 3. XRD patterns of the TiO_2 nanotube arrays electrodes obtained at different temperature

3.2. Photoelectrochemical performance

Fig. 4(a) showed I-V property of the electrodes, and it could be seen that photocurrents increased with the applied voltage and reached a platform under a certain potential. It should be noted that the dark current was close to zero without the light for all electrodes (dark line). This suggested that the electrodes could generate photoinduced charge carriers under the illumination. Fig. 4(b) displayed the plot of i_{ph}^2

with respect to the applied potential (the original data were obtained from the I-V curve of Fig. 4(a)). It was discovered that all electrodes showed fine linearity in a narrow potential range. The voltage range was ca. 0.5 V for T-30°C, T-40°C and T-50°C electrode. However, the potential range increased to ca. 0.7 V for T-60°C. According to the literature[38], the compact TiO₂ films with a thick layer generally exhibited reasonable linearity in an extended potential range. This implied that the space charge layer within the nanotube wall could not be maintained at a relatively high voltage, which can be attributed to the restriction of its wall thickness rather than the layer thickness that is equal to the length of nanotube. The consequence revealed that the limiting photocurrent may be controlled by electron migration through a space charge layer when the applied voltage exceeded the critical potential.

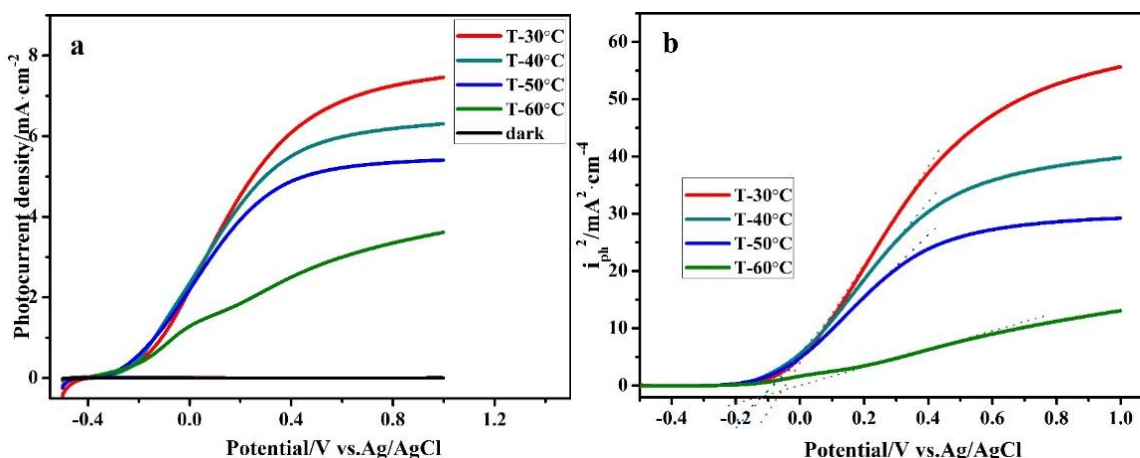


Figure 4. (a) I-V curves of the as-prepared electrodes in 0.1 M Na₂SO₄ aqueous solutions; (b) Plot of photocurrent density to the square i_{ph}^2 vs applied potential for samples, based on curve (a)

EIS measurement was conducted to analyze the charge transport process. Fig. 5 showed EIS response of the as-synthesized electrodes. The equivalent circuit (as shown in Fig. 5) was proposed as the model for the present system and the solid lines were the simulated results. We employed the constant phase angle element (CPE) to substitute the capacitance because of the inhomogeneous surface on nanoporous electrode. This model adequately fitted the experimental data. It was well known that the interfacial resistance showed a positive relationship with the radius of arc.

From Fig. 5, we observed that the charge transport resistance (R_{ct}) rose with the increasing temperature. Table 1 showed the fitted equivalent circuit data from the impedance spectra. The R_{ct} increased from 198.5 $\Omega \cdot \text{cm}^{-2}$ (T-30°C) to 487.3 $\Omega \cdot \text{cm}^{-2}$ (T-60°C) and the space charge layer capacitance (C_{sc}) decreased from $8.50 \times 10^{-5} \text{ F} \cdot \text{cm}^{-2}$ (T-30°C) to $5.09 \times 10^{-5} \text{ F} \cdot \text{cm}^{-2}$ (T-60°C). The enhanced resistance and attenuated capacitance resulted in the growth of R_{ct} . From SEM we found that some nanowires appeared on electrode surface when the preparation temperature was higher than 40°C. The irregular nanowires structure provided more recombination sites for photogenerated electrons-holes pairs, which caused a decline of charge separation efficiency. Therefore, the charge transfer on electrode surface became more difficult for electrode fabricated at higher temperature.

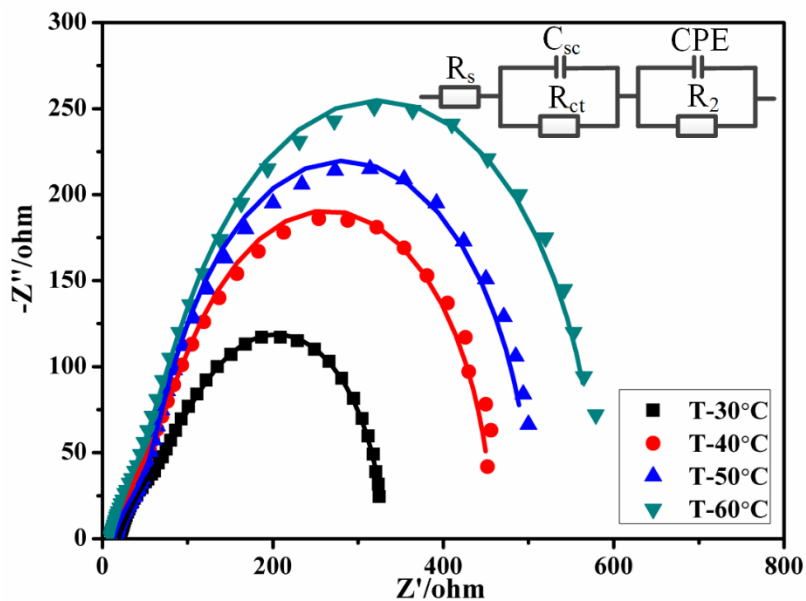


Figure 5. EIS curves of the electrodes obtained at different temperature in 0.1 M Na₂SO₄ aqueous solutions under open circuit

Table 1. Fitted equivalent circuit data from the impedance spectra

samples	$R_s/\Omega \cdot \text{cm}^{-2}$	$R_{ct}/\Omega \cdot \text{cm}^{-2}$	$C_{sc}/\text{F} \cdot \text{cm}^{-2}$	$R_2/\Omega \cdot \text{cm}^{-2}$	$\text{CPE}/\text{S} \cdot \text{sec}^n \cdot \text{cm}^{-2}$	n
T-30°C	18.66	198.5	8.50×10^{-5}	115.2	1.66×10^{-4}	0.80
T-40°C	12.77	357.90	5.08×10^{-5}	87.35	1.33×10^{-4}	0.80
T-50°C	13.32	428.80	5.75×10^{-5}	61.83	1.50×10^{-4}	0.80
T-60°C	10.66	487.3	5.09×10^{-5}	83.90	1.67×10^{-4}	0.80

Potentiostatic photocurrent (I-t) measurement under intermittent illumination of the electrodes was shown in Fig. 6. It was found that all electrodes exhibited excellent photoresponse performance, and the photocurrents increased and dropped immediately during light on/off cycles. This suggested a rapid charge transport for all electrodes. The average photocurrent was $6.64 \text{ mA} \cdot \text{cm}^{-2}$, $5.87 \text{ mA} \cdot \text{cm}^{-2}$, $5.03 \text{ mA} \cdot \text{cm}^{-2}$, $2.88 \text{ mA} \cdot \text{cm}^{-2}$ for T-30°C, T-40°C, T-50°C and T-60°C samples, respectively. The photocurrent decreased with the fabrication temperature.

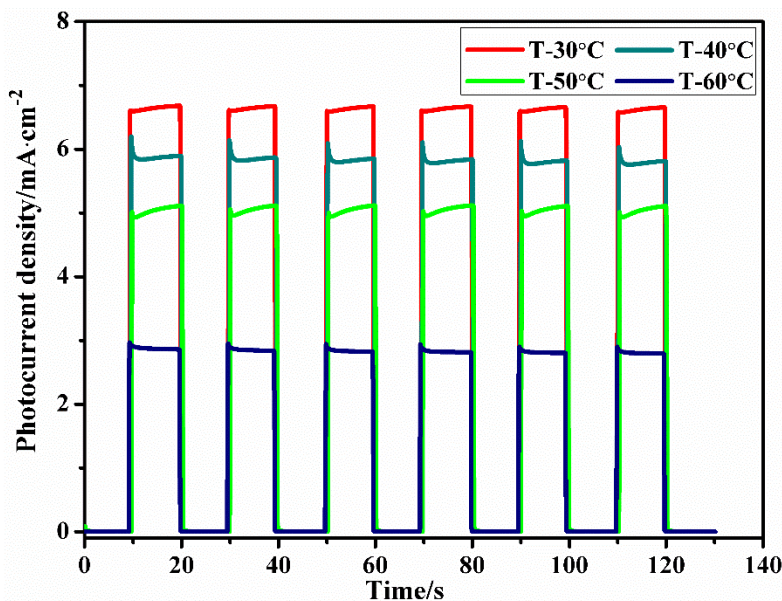


Figure 6. I-t curves of the electrodes in 0.1 M Na₂SO₄ aqueous solutions

To obtain a better perception of the correlation between photocurrent and the specific nanotube structure, Mott-Schottky curve was plotted for the as-prepared samples. Fig. 7(a) shows the relationship between capacitance and potential. The donor concentration (N_D) and the flat band potential (V_{fb}) in electrochemical system can be determined by fitting C_{sc}^{-2} versus V according to equation (1), as shown in Fig. 7(b).

$$C_{sc}^{-2} = (2/\epsilon\epsilon_0eN_D)(V - V_{fb} - kT/e) \quad (1)$$

where C_{sc} represents the capacitance of the space charge layer; ϵ is the dielectric constant of the semiconductor (for anatase TiO₂, ϵ is 42); ϵ_0 is the vacuum permittivity, e is the electron charge; V is the applied potential; k is the Boltzmann constant; T is the absolute temperature.

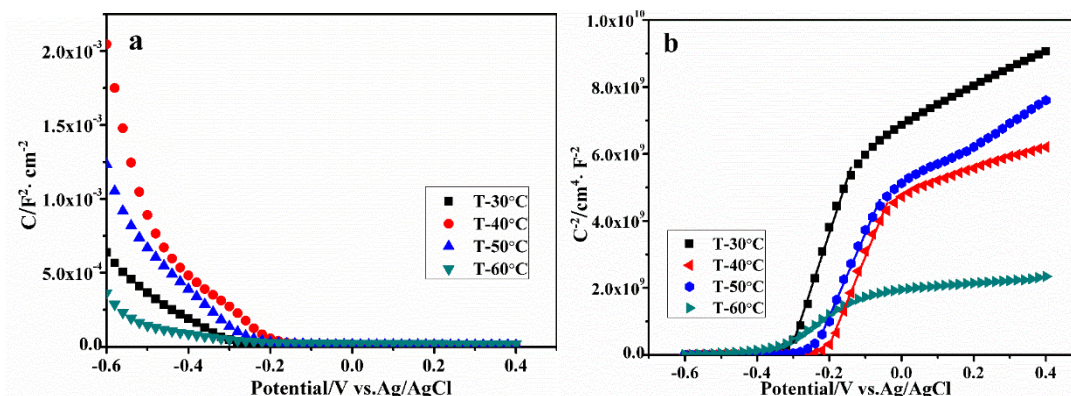


Figure 7. Mott-Schottky curve of the electrodes in 0.1 M Na₂SO₄

The V_{fb} was -0.34 V, -0.24 V, -0.27 V, and -0.39 V for T-30°C, T-40°C, T-50°C and T-60°C electrode, respectively. The variation of V_{fb} was in relation to the crystal structure. The N_D was 1.03×10^{20}

cm^{-3} , $1.26 \times 10^{20} \text{ cm}^{-3}$, $1.35 \times 10^{20} \text{ cm}^{-3}$, $4.68 \times 10^{20} \text{ cm}^{-3}$ for T-30°C, T-40°C, T-50°C and T-60°C electrode, respectively. It was found that N_D increased with the increasing preparation temperature. This could be attributed to the formation of nanowires caused by redissolution of the nanotube on top surface.

According to Gärtner model[37], the observed photocurrent (i_{ph}) was represented in the equation (2):

$$i_{ph} = eJ_0[1 - \exp(-\alpha W_{sc})] \quad (2)$$

where J_0 is the intensity of the incident light flux; α is the optical adsorption coefficient; W_{sc} is the width of the space charge layer. For an n-type semiconductor, W_{sc} can be calculated by the equation (3):

$$W_{sc} = [(2\epsilon\epsilon_0/eN_D)(V - V_{fb} - kT/e)]^{1/2} \quad (3)$$

The calculated W_{sc} is 6.1 nm, 5.2 nm, 5.2 nm, and 3.0 nm for T-30°C, T-40°C, T-50°C and T-60°C electrode, respectively. From equation (2) we can observe that i_{ph} increases with an increase in the width of the space charge layer. This phenomenon explains the change of photocurrent in Fig. 6.

3.3. Photoelectrocatalytic activity

RhB degradation was carried out to investigate the photoelectrocatalytic activity of the as-prepared samples, as shown in Fig. 8. It was obvious that T-30°C showed the best degradation efficiency. This result was in accordance with EIS measurement and I-t test, which suggested that the electrode fabricated at higher temperature was not favorable for RhB degradation. From Fig. 8(b) we observed that the RhB degradation kinetics were found to follow the pseudo-first-order decay kinetics (k). There were two degradation constants for T-30°C ($k_{30-1} = 0.0378 \text{ min}^{-1}$, $k_{30-2} = 0.0460 \text{ min}^{-1}$), T-40°C ($k_{40-1} = 0.0226 \text{ min}^{-1}$, $k_{40-2} = 0.0654 \text{ min}^{-1}$), T-50°C ($k_{50-1} = 0.0162 \text{ min}^{-1}$, $k_{50-2} = 0.0302 \text{ min}^{-1}$) and one degradation constant for T-60°C ($k_{60} = 6.03 \times 10^{-3} \text{ min}^{-1}$). The catalyst with similar photoelectrocatalysts for RhB degradation in literature are listed in Table 2. For instance, H. Safajou et al [40] used the TiO_2 NWs and TiO_2 NPs to degrade RhB. The result showed that the efficiency after 40-min degradation of RhB was 62% for TiO_2 NPs, 66% for TiO_2 NWs. Hao et al [41] use the g- $\text{C}_3\text{N}_4/\text{TiO}_2$ heterojunction photocatalysts to degrade RhB. The k value achieved a maximum of $36.7 \times 10^{-3} \text{ min}^{-1}$, at a melamine content of 3 g. Compared with these works, the degradation rate and the apparent reaction rate constants and of RhB for this work is obviously excellent.

Table 2. The catalyst with similar photoelectrocatalysts for RhB degradation in literature

Photocatalyst	Degradation condition	Light source	Degradation efficiency	Ref.
Flower-like rutile TiO_2 superstructures	Photocatalyst: 0.1 g; RhB: 100 mL 5 mg/L; Degradation time: 20 min	15 W UV lamp (concentrated at 275 nm)	Degradation efficiency: Almost decomposed completely; Degradation constants: $171.6 \times 10^{-3} \text{ min}^{-1}$	[17]
Graphene/Pd/ TiO_2 nanocomposites	Photocatalyst: 0.03 g; RhB: 40 mL 10 mg/L; Degradation time: 40 min	400W Mercury lamp	Degradation efficiency: 79% (Gr/Pd/ TiO_2 -NPs), 90% (Gr/Pd/ TiO_2 -NWs);	[40]

g-C ₃ N ₄ /TiO ₂ heterojunction	Photocatalyst:0.04 g; RhB: 30 mL 1×10 ⁻⁵ M; Degradation time:80 min	350 W Xenon arc lamp with UV-cutoff filter (420 nm)	Degradation constants: No data Degradation efficiency: 95.2%; Degradation constants: 36.7×10 ⁻³ min ⁻¹	[41]
M@TiO ₂ (M= Au, Pd, Pt)	Photocatalyst:30 mg; RhB:60 mL 1×10 ⁻⁵ mol/L; Degradation time:5 h(λ >400 nm);4 h(λ =365±15 nm)	300 W Xenon lamp equipped with a filter to cut off light of wavelength below 400 nm (λ >400 nm) or center the wavelength of the incident light at 365 nm (±15 nm)	Degradation efficiency: Almost decomposed completely; Degradation constants:2.29 h ⁻¹ (λ >400 nm, Pd@TiO ₂);4.77 h ⁻¹ (λ =365±15nm, Pt@TiO ₂)	[42]
Heterogeneous TiO ₂ P-25/EO/RhB system	Photocatalyst:50 mg P-25, 20 mg/L EO; RhB: 100 mL 4 mg/L; Degradation time:35 min	300 W Xe lamp equipped with a 420 nm cut off filter	Degradation efficiency: Almost decomposed completely; Degradation constants: No data	[43]
In ₂ O ₃ /TiO ₂ nanotube arrays	Photocatalyst:Active area of 1×3 cm ² ; RhB: 3 mL 10 mg/L; Degradation time:2 h	300W Xe lamp with a 365 nm cut-off filter	Degradation efficiency: 77%; Degradation constants: No data	[44]
Au nanoparticle modified three-dimensional network PVA/RGO/TiO ₂ composite	Photocatalyst:0.05g; RhB: 50 mL 10 mg/L; Degradation time:60 min	150 W high-pressure sodium lamp	Degradation efficiency: 92%; Degradation constants: 0.03851 min ⁻¹	[45]
Pt quantum dots on TiO ₂ nanotube arrays	Photocatalyst: Active area was not mentioned; RhB: 20 mL 5 mg/L; Degradation time:180 min	300 W Xenon lamp with the 365 nm filter	Degradation efficiency: 73.47%; Degradation constants: 7.19×10 ⁻³ min ⁻¹	[46]
TiO ₂ /Carbon Nanotubes/Reduced Graphene Oxide Composites	Photocatalyst:10 mg; RhB: 60 mL 10 mg/L; Degradation time:60 min	300 W Xenon lamp	Degradation efficiency: Almost decomposed completely; Degradation constants: 0.08785 min ⁻¹	[47]
Bismuth-doped TiO ₂ nanotubes	Photocatalyst:0.05 g; RhB: 100 mL 50 mg/L; Degradation time:3 h	Direct sunlight irradiation in the month of April–May 2011	Degradation efficiency: 100%; Degradation constants: 6.2×10 ⁻³ min ⁻¹	[48]
Ti ³⁺ self-doped TiO ₂ @Ag nanoparticles	Photocatalyst:50 mg; RhB: 60 mL 20 mg/L; Degradation time:60 min	300 W Xenon lamp equipped with a UV cut-off filter(λ >420 nm)	Degradation efficiency: 97.76%; Degradation constants: 0.068 min ⁻¹	[49]
TiO ₂ nanotubes (30 °C)	Photocatalyst: Active area of 2×2 cm ² ; RhB: 10 mg/L; Degradation time:2 h	375 nm LED monochromatic source	Degradation efficiency: 95%; Degradation constants: 0.0378 min ⁻¹ and 0.0460 min ⁻¹	This work

Previous research demonstrated that the degradation rate was sensitive to the photogenerated carriers and the second rate constant disappeared due to the confine of photogenerated carriers [50]. Obviously, the RhB degradation rate for T-30°C was faster than that for T-40°C, T-50°C and T-60°C. This can be ascribed to the high separation efficiency of photoelectrons-holes pairs. Fig. 8(c) shows total COD removal of the as-synthesized samples, indicating that COD removal efficiency was 95.0%, 91.3%, 72.6%, and 40.7% for T-30°C, T-40°C, T-50°C, and T-60°C, respectively. Based on the above results, we speculated that TiO₂ nanotube arrays electrodes synthesized at higher temperature exhibited a nanowire/nanotube composite structure and a high donor concentration. The irregular nanowires and high N_D provided more recombination site for photogenerated electrons-holes pairs, resulting in a decrease of photoelectrocatalytic performance. On the other hand, the photoelectrochemical measurements revealed that T-30°C had a higher photocurrent and a fast charge transfer, which implied an enhanced photoelectrocatalytic activity. In summary, T-30°C electrode exhibited the best photoelectron degradation property due to its fast charge transfer and high separation efficiency of photogenerated electrons-holes pairs.

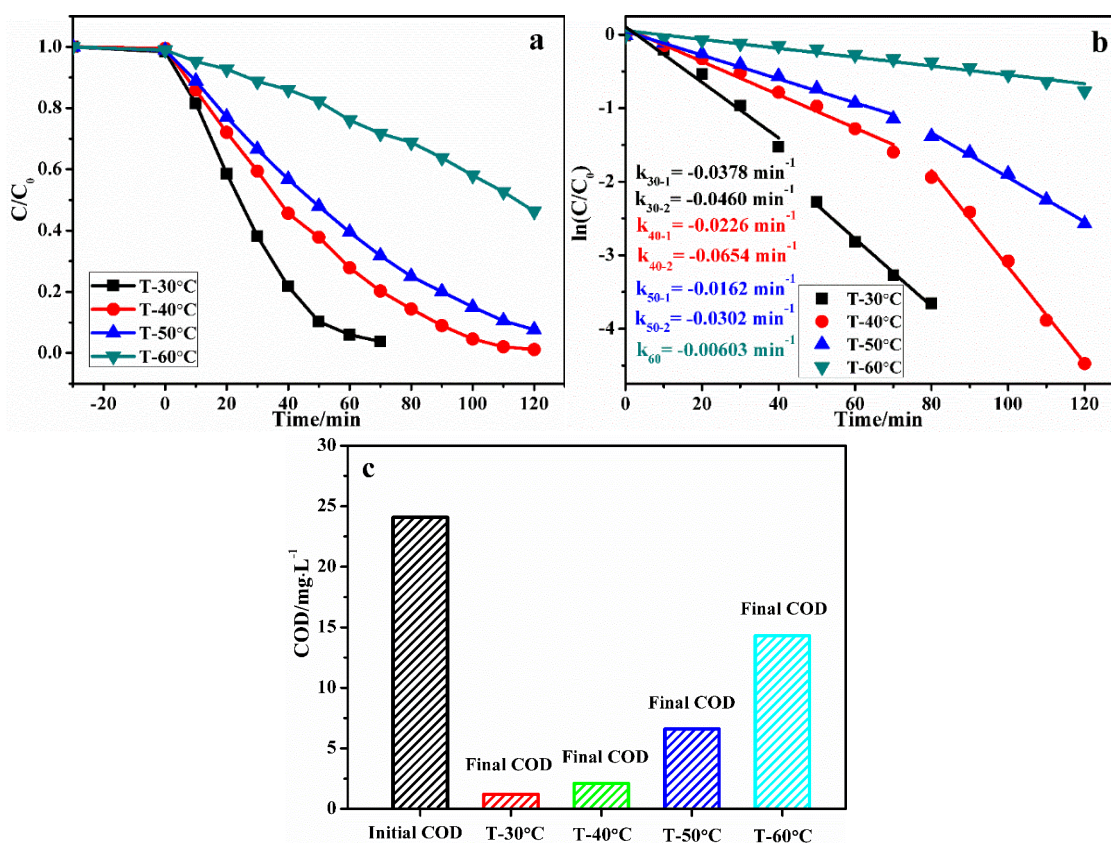


Figure 8. (a) RhB photoelectrodegradation efficiencies of the electrodes. (b) The corresponding kinetics of RhB degradation. (c) Total COD removal of different electrodes

3.4. Stability of the electrode

The stability of degradation performance for the removal of organic pollutant is one of the most important factors to determine the catalyst practical application potential [41]. From the above results,

we observed that T-30°C electrode exerted the best photoelectrocatalytic performance. To estimate its reusability and stability, RhB photoelectron degradation in recycle was also investigated, as shown in Fig. 9. In each cycle, T-30°C electrode was exposed to 40 mL supporting electrolytes. It was found that there was no remarkable loss of activity after six cycles and RhB was almost completely decomposed in each cycle confirming that the electrode was stable during the photoelectrocatalytic degradation process.

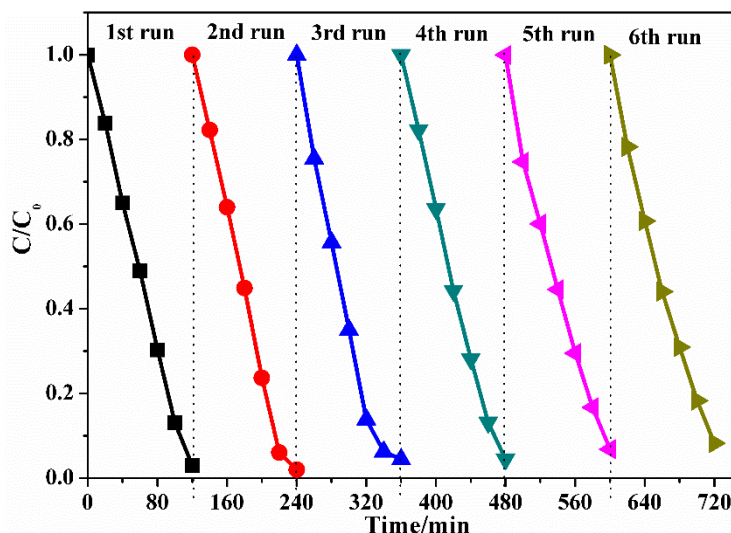


Figure 9. RhB photoelectrocatalytic degradation in six cycles on TiO₂ nanotube arrays electrode

3.5. RhB degradation mechanism

To clarify the main reactive species in photoelectrocatalytic process, the trapping experiments was conducted on T-30°C. Fig. 10 showed the variation of degradation rates in the presence of different scavengers. It can be clearly observed from Fig. 10 that different scavengers have different influences on the photodegradation of RhB over the T-30°C sample [39]. It was observed that degradation rate was strongly depressed after adding KI (a quencher of holes (h⁺) and ·OH) to the solutions. This suggested that RhB was mainly degraded by the holes and/or ·OH. To identify the roles of them, t-BuOH was employed as a scavenger of ·OH. It was found that total degradation efficiency first increased with time because of the interaction between holes and ·OH. This indicated that holes played a role in the formation of ·OH at the first stage. The trapping of ·OH increased the accumulation of the holes, thus enhanced the photoelectrocatalytic activity. As the degradation proceed, the generation of ·OH was not limited by holes. Therefore, the degradation efficiency decreased with time due to the trapping of ·OH. This suggested that ·OH played a certain role in RhB degradation. Moreover, BQ (1 mmol·L⁻¹) was employed for trapping ·O₂⁻ during the RhB degradation. It can be seen that degradation rate was reduced with the increase of degradation time, which suggested that ·O₂⁻ can accelerate the photoelectrocatalytic process in the later period. To investigate the effect of electrons (e⁻) during the degradation, K₂S₂O₈ (10 mmol·L⁻¹) were added to the solutions, then the RhB degradation efficiency was improved. This phenomenon can be attributed to the accumulation of holes due to the consumption of electron. Therefore, we

concluded that the main reactive species was h^+ , and the formation of $\cdot O_2^-$ or $\cdot OH$ in the later period during RhB degradation was also beneficial for photoelectrocatalytic process.

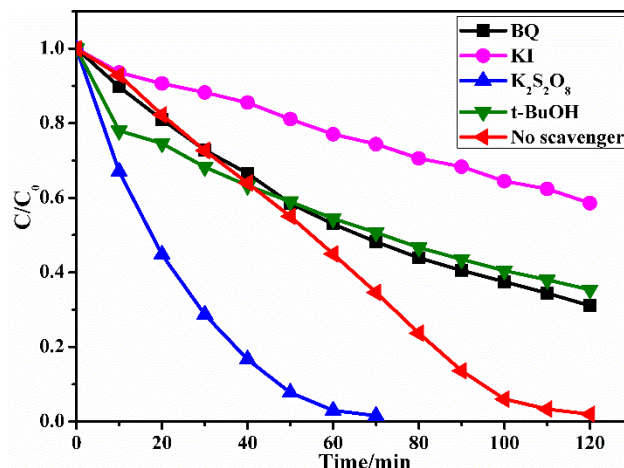


Figure 10. Effect of different scavengers on photoelectrocatalytic activity of TiO₂ nanotube arrays electrode

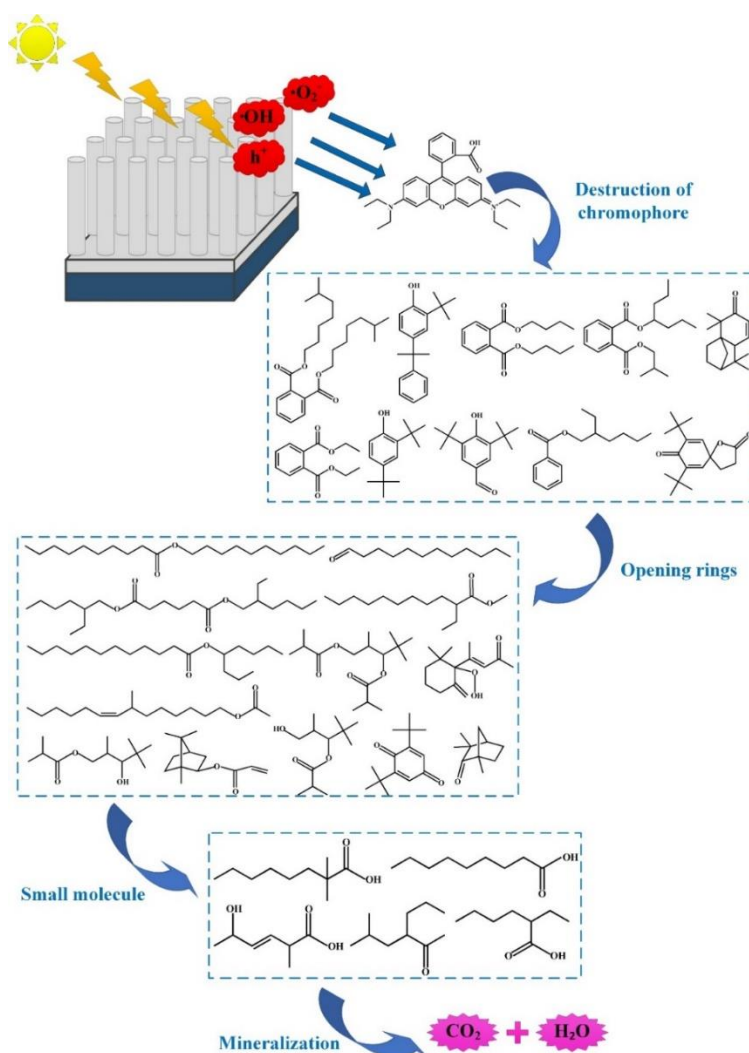


Figure 11. Proposed photoelectrocatalytic degradation mechanism of RhB on TiO₂ nanotube arrays electrode

To fully perceive the photoelectron degradation pathway, the intermediates during the degradation process were analyzed by GC–MS. To ensure the accuracy of the analysis, the samples were enriched with a solid phase microextraction system before the GC–MS test. The GC–MS results indicated that intermediates containing benzene or heterocyclic compounds were generated in the initial stage due to the destruction of conjugated chromotropic structures. These products were subsequently degraded to long chains esters or ketones by opening rings due to the attack of active radicals. With the assistance of reactive species, the esters or ketones compounds were further converted to smaller carboxylic acids or esters, and were eventually degraded to carbon dioxide and water. Fig.11 illustrated the proposed mechanism for RhB photoelectrocatalytic degradation under illumination. The degradation process went through the following stages: damage of conjugated chromophoric to form benzene rings or poly-heterocyclic compounds; opening of rings to produce ester or ketone; breaking of longer chains to form smaller molecules (carboxylic acids or esters); mineralization to carbon dioxide and water.

4. CONCLUSION

In this work, TiO₂ nanotube arrays electrodes have been successfully prepared by anodization approach at different temperature. SEM and XRD results revealed that temperature can affect the morphology and structure. The nanowires/nanotube arrays composite structure appeared at higher temperature. Moreover, the nanotube length and crystal structure varied with the temperature. I-V and I-t measurements showed that the photocurrent decreased with increasing the preparation temperature, which can be attributed to the decrease of W_{sc} . Mott-Schottky plot indicated the change of V_{fb} , N_D and W_{sc} for the as-synthesized electrodes and further explained the reason for photocurrent variation. RhB photoelectrocatalytic degradation was carried out to understand the photoelectrocatalytic activity. It was found that T-30°C electrode exhibited the best catalytic activity and a strong stability. This can be ascribed to the fast charge transport and charge separation efficiency. Finally, the main reactive species and degradation mechanism during the photoelectrodegradation process were also investigated. It was observed that the main reactive species was h^+ , and the generation of $\cdot O_2^-$ or $\cdot OH$ in the later period was also favorable for RhB degradation. The probable photoelectron degradation mechanism was proposed by employing SPME-GC-MS technique. The degradation pathway mainly contained destruction of conjugated chromophoric, opening rings, producing small molecules and mineralization. In summary, these results demonstrated the influence of temperature on synthesis and photoelectrochemical performance of TiO₂ nanotube-based photoelectrodes. Moreover, the work also provided a specific RhB photoelectrocatalytic degradation pathway. These findings were favorable for investigating the performance of TiO₂ nanotube arrays electrode and further understanding the photoelectrocatalytic process.

ACKNOWLEDGMENTS

The authors gratefully acknowledge the financial support from the Key R&D Programs in Shaanxi Province (Program No. 2018SF-372) and Water Science and Technology Projects Foundation of SWAG

(Program No. 2018SWAG0203). Thanks Mr. Xu Zhicheng for his contribution to the language modification of this paper.

References

1. H. Li, N. Tang, H. Yang, X. Leng and J. Zou, *Appl. Surf. Sci.*, 355 (2015) 849.
2. L. Wang, Z. Nie, C. Cao, M. Ji, L. Zhou and X. Feng, *J. Mater. Chem. A*, 3 (2015) 3710.
3. M. Abdullah and S.K. Kamarudin, *Renew. Sust. Energ. Rev.* 76 (2017) 212.
4. S. Rani, S.C. Roy, M. Paulose, O.K. Varghese, G.K. Mor, S. Kim, S. Yoriya, T.J. LaTempa and C.A. Grimes, *Phys. Chem. Chem. Phys.*, 12 (2010) 2780.
5. Q. Zhang, V. Celorrio, K. Bradley, F. Eisner, D. Cherns, W. Yan and D.J. Fermín, *J. Phys. Chem. C*, 118 (2014) 18207.
6. X. Zeng, Y.X. Gan, E. Clark and L. Su, *J. Alloy. Compd.*, 509 (2011) L221.
7. J. Wu, H. Xu and W. Yan, *J. Alloy. Compd.*, 691 (2017) 388.
8. D.T. Zhou, Z. Chen, T. Gao, F. Niu, L.S. Qin and Y.X. Huang, *Energy Technol.*, 3 (2015) 888.
9. Y. Liu, H. Zhou, B. Zhou, J. Li, H. Chen, J. Wang, J. Bai, W. Shanguan and W. Cai, *Int. J. Hydrog. Energy.*, 36 (2011) 167.
10. J. Wang and Z.Q. Lin, *Chem.-Asian J.*, 7 (2012) 2754.
11. A.F. Kanta, M. Poelman and A. Decroly, *Sol. Energ. Mat. Sol. C.*, 133 (2015) 76.
12. S. So, K. Lee and P. Schmuki, *Chem.-Eur. J.*, 19 (2013) 2966.
13. W.T. Kim, I.H. Kim and W.Y. Choi, *J. Nanosci. Nanotechnol.*, 15 (2015) 8161.
14. Y.L. Liu, L.L. Wang, H.R. Wang, M.Y. Xiong, T.Q. Yang and G.S. Zakharova, *Sens. Actuator B-Chem.*, 236 (2016) 529.
15. M.H. Zarifi, S. Farsinezhad, M. Abdolrazzagli, M. Daneshmand and K. Shankar, *Nanoscale*, 8 (2016) 7466.
16. P. Dwivedi, N. Chauhan, P. Vivekanandan, S. Das, D.S. Kumar and S. Dhanekar, *Sens. Actuator B-Chem.*, 249 (2017) 602.
17. S. Ge, B. Wang, D. Li, W. Fa, Z. Yang, Z. Yang, G. Jia and Z. Zheng, *Appl. Surf. Sci.*, 295 (2014) 123.
18. R. Li, Q.Y. Li, L.L. Zong, X.D. Wang and J.J. Yang, *Electrochim. Acta*, 91 (2013) 30.
19. J. Wu, H. Xu and Y. Wei, *RSC Adv.*, 5 (2015) 19284.
20. W. Han, C. Zhong, L. Liang, Y. Sun, Y. Guan, L. Wang, X. Sun and J. Li, *Electrochim. Acta*, 130 (2014) 179.
21. M. Alfè, D. Spasiano, V. Gargiulo, G. Vitiello, R.D. Capua and R. Marotta, *Appl. Catal. A-Gen.*, 487 (2014) 91.
22. R. Fazaeli, H. Aliyan, S. Tangestaninejad and S.P. Foroushani, *J. Iran. Chem. Soc.*, 11 (2014) 1687.
23. C. Hu, F. Chen, T. Lu, C. Lian, S. Zheng, Q. Hu, S. Duo and R. Zhang, *Appl. Surf. Sci.*, 317 (2014) 648.
24. Y. Xue, Y. Sun, G. Wang, K. Yan and J. Zhao, *Electrochim. Acta*, 155 (2015) 312.
25. Q. Zhang, H. Xu and W. Yan, *Nanosci. Nanotechnol. Lett.*, 4 (2012) 505.
26. Y. Lai, H. Zhuang, L. Sun and C. Lin, *Electrochim. Acta*, 54 (2009) 6536.
27. L.J. Qin, Q.J. Chen, R.J. Lan, R.Q. Jiang, X. Quan, B. Xu, F. Zhang and Y.M. Jia, *J. Mater. Sci. Technol.*, 31 (2015) 1059.
28. X. Yuan, M. Zheng, L. Ma and W. Shen, *Nanotechnology*, 21 (2010) 405302.
29. D. Guan and Y. Wang, *Nanoscale*, 4 (2012) 2968.
30. S.P. Albu, A. Ghicov, S. Aldabergenova, P. Drechsel, D. Leclere, G.E. Thompson, J.M. Macak and P. Schmuki, *Adv. Mater.*, 20 (2010) 4135.
31. T. Soltani and M.H. Entezari, *Chem. Eng. J.*, 223 (2013) 145.
32. B. Pan, Y. Xie, S. Zhang, L. Lv and W. Zhang, *ACS Appl. Mater. Interfaces*, 4 (2012) 3938.

33. H.Y. Yang, S.F. Yu, S.P. Lau, X.W. Zhang, D.D. Sun and G. Jun, *Small*, 5 (2009) 2260.
34. U.G. Akpan and B.H. Hameed, *J. Hazard. Mater.*, 170 (2009) 520.
35. J. Wu, H. Xu and W. Yan, *Appl. Surf. Sci.*, 386 (2016) 1.
36. J.H. Lim and J. Choi, *Small*, 3 (2007) 1504.
37. H. Xu, Q. Zhang, C. Zheng, W. Yan, W. Chu, *Appl. Surf. Sci.*, 257 (2011) 8478.
38. J. Georgieva, S. Armyanov, E. Valova, I. Poullos and S. Sotiropoulos, *Electrochim. Acta*, 51 (2006) 2076.
39. X. Wu, Y. Ling, L. Li and Z. Huang, *J. Electrochem. Soc.*, 156 (2009) K65.
40. H. Sagajou, H. Khojasteh, M. Salavati-Niasari and S. Mortazavi-Derazkola, *J Colloid Interf. Sci.*, 498 (2017) 423.
41. R. Hao, G. Wang, C. Jiang, H. Tang and Q. Xu, *Appl. Surf. Sci.*, 411 (2017) 400.
42. N. Zhang, S. Liu and X. Fu, *J. Phys. Chem. C*, 115 (2011) 9136.
43. M. Yin, Z. Li and J. Kou, *Environ. Sci. Technol.*, 43 (2009) 8361.
44. C. Xiao, Z. Tan, C. Wang, X. Yang, G. Zhang and H. Pan, *Mater. Res. Bull.*, 106 (2018) 197.
45. L. Zhang, H. Qi, Y. Zhao, L. Zhong, Y. Zhang, Y. Wang, J. Xue and Y. Li, *Appl. Surf. Sci.*, 498 (2019) 143855.
46. Y. Wang, Y. Zhu, X. Zhao, X. Yang, X. Li, Z. Chen, L. Yang, L. Zhu, T. Gao and Z. Sha, *Surf. Coat. Technol.*, 281 (2015) 89.
47. Y. Huang, D. Chen, X. Hu, Y. Qian and D. Li, *Nanomaterials*, 8 (2018) 431.
48. T. S. Natarajan, K. Natarajan, H. C. Bajaj and R. J. Tayade, *J. Nanopart. Res.*, 15 (2013) 1669.
49. W. Yang, H. Shen, H. Min and J. Ge, *J. Mater. Sci.*, 55 (2020) 701.
50. Y. Deng, M. Xing and J. Zhang, *Appl. Catal. B-Environ.*, 211 (2017) 157.